

Mass and density of the transiting hot and rocky super-Earth LHS 1478 b (TOI-1640 b)

M. G. Soto^{1*}, G. Anglada-Escudé^{1,2,3}, S. Dreizler⁴, K. Molaverdikhani^{5,6}, J. Kemmer⁵, C. Rodríguez-López⁷, J. Lillo-Box⁸, E. Pallé^{9,10}, N. Espinoza¹¹, J. A. Caballero⁸, A. Quirrenbach⁵, I. Ribas^{2,3}, A. Reiners⁴, N. Narita^{12,13,14,9}, T. Hirano^{15,14,16}, P. J. Amado⁷, V. J. S. Béjar^{9,10}, P. Bluhm⁵, C. J. Burke²⁶, D. A. Caldwell^{17,18}, D. Charbonneau¹⁹, R. Cloutier¹⁹, K. A. Collins¹⁹, M. Cortés-Contreras⁸, E. Girardin²⁰, P. Guerra²¹, H. Harakawa²², A. P. Hatzes²³, J. Irwin¹⁹, J. M. Jenkins¹⁸, E. Jensen²⁴, K. Kawauchi¹⁵, T. Koyati^{14,16,25}, T. Kudo²², M. Kunitomo²⁶, M. Kuzuhara^{14,16}, D. W. Latham¹⁹, D. Montes²⁷, J. C. Morales^{2,3}, M. Mori²⁸, R. P. Nelson¹, M. Omiya^{14,16}, S. Pedraz²⁹, V. M. Passegger^{30,31}, B. Rackham³², A. Rudat²⁶, J. E. Schlieder³³, P. Schöfer⁴, A. Schweitzer³⁰, A. Selezneva²¹, C. Stockdale³⁴, M. Tamura^{28,14,16}, T. Trifonov⁶, R. Vanderspek²⁶, and D. Watanabe³⁵

(Affiliations can be found after the references)

Received dd February 2021 / Accepted dd Month 2021

ABSTRACT

One of the main objectives of the *Transiting Exoplanet Survey Satellite* (TESS) mission is the discovery of small rocky planets around bright, nearby stars. Here, we report the confirmation and characterization of the transiting super-Earth planet orbiting LHS 1478 (TOI-1640). The star is an inactive red dwarf ($J = 9.6$ mag and spectral type M3.5 V) with mass and radius estimates of $0.20 \pm 0.01 M_{\odot}$ and $0.25 \pm 0.01 R_{\odot}$, respectively, and an effective temperature of 3381 ± 54 K. It was observed by TESS in four sectors. These data revealed a transit-like feature with a period of 1.949 days. We combined the TESS data with three ground-based transit measurements, 57 radial-velocity (RV) measurements from CARMENES, and 13 RV measurements from IRD to determine that the signal is produced by a planet with a mass of $2.33^{+0.20}_{-0.20} M_{\oplus}$ and radius $1.24^{+0.05}_{-0.05} R_{\oplus}$. The resulting bulk density of this planet is 6.66 g cm^{-3} , consistent with a rocky planet with a Fe- and MgSiO₃-dominated composition. Although the planet would be too hot to sustain liquid water on its surface (its equilibrium temperature is of about ~ 595 K), spectroscopic metrics based on the capabilities of the forthcoming *James Webb Space Telescope*, and the fact that the host star is rather inactive indicate that this is one of the most favorable known rocky exoplanets for atmospheric characterization.

Key words. planets and satellites: detection - planets and satellites: fundamental parameters - techniques: photometric - techniques: radial velocities

1. Introduction

Stars smaller than the Sun offer a number of advantages for the detection of exoplanets with both the Doppler (e.g. Proxima b, Anglada-Escudé et al. 2016) and the photometric transit methods (e.g. the TRAPPIST-1 system, Gillon et al. 2017). Both are indirect methods that rely on the planet imprinting a signal onto the star-light. The Doppler technique measures the radial velocity of the star by measuring to high accuracy the wavelength shift of numerous absorption features in the stellar spectrum. The amplitude of the signal is larger for a larger planet-star mass ratio and for short orbital periods. The transit method relies on measuring the light blocked by the planet as it crosses the stellar disk. In this case the signal is proportional to the planet-star surface area ratio, and it repeats once per orbital period. In both methods, short-period planets are therefore more easily detectable.

Exoplanet surveys with the Doppler technique are typically conducted with ground-based high-resolution spectrometers ($R = \lambda/\delta\lambda > 50\,000$) that are kept in a very stable environment and are calibrated against spectral features of a reference source measured in the laboratory. This is the case for the CARMENES (Quirrenbach et al. 2016) spectrometer, which was specifically designed to obtain maximal precision on red-dwarf stars. The CARMENES survey has led to numerous new exo-

planet discoveries in the super-Earth down to Earth mass regime, in hot to warm temperate orbits (e.g. Luque et al. 2018; Zechmeister et al. 2019; Stock et al. 2020). Several of these planets have been detected both in transit and by radial velocities (Luque et al. 2019; Dreizler et al. 2020; Kemmer et al. 2020; Nowak et al. 2020; Bluhm et al. 2020). On the other side, the NASA *Transiting Exoplanet Survey Satellite* mission (TESS, Ricker et al. 2015) has been surveying most of the sky for signals of transiting planets, with the goal of detecting those that should enable a more straightforward atmospheric characterization. To date, TESS has revealed numerous exoplanet candidates transiting nearby M dwarfs (Astudillo-Defru et al. 2020; Dreizler et al. 2020; Gan et al. 2020; Kanodia et al. 2020, to give a few).

One key element in the characterization and study of transiting planets is their validation using Doppler spectroscopy, which in turn produces a measurement of their masses, allowing us to derive their mean bulk densities and put constraints on their composition. Finally, the atmospheres of transiting planets can be studied by performing spectroscopic measurements during transits (the planet blocks more light at certain wavelengths where the molecules in its atmosphere deter more light producing deeper transits), and secondary eclipses (the spectrum of thermal emission of the planet is also affected by the presence of absorbing molecules, producing a shallower dip in the light curve when the planet goes behind the star). Among these,

* E-mail: m.soto@qmul.ac.uk

and thanks to the more favorable radius ratio between the planet and the star, exoplanets transiting red-dwarfs are the best ones for atmospheric characterization. The measured spectrum of an exoplanet can be affected by the presence of spots and active regions in the visible part of the star during transits (Rackham et al. 2018): the less active the star is, the cleaner and easier to interpret is the measured spectrum of a planet.

Due to its properties (transiting, Doppler signal in the few m/s regime), and host star (small, relatively nearby and low stellar activity), LHS 1478 satisfies *all* the favorable conditions to become a prime target for characterization of rocky terrestrial planets.

In this paper, we validate the transiting exoplanet LHS 1478 b (TOI-1640 b). We provide an overview of the measurements with photometry (initial detection, stellar activity, orbital period and planet size), imaging (validation against false positives), and radial velocity (confirmation, stellar activity, and measurement of the planet mass) in Sec. 2. Stellar parameters are revised in 3.1, and a joint analysis to constrain the planet properties is given in Sec. 3.2. We discuss the results in the context of terrestrial planet candidates and further follow-up in Sec. 4, and summarize our work in Sec. 5.

2. Data

2.1. TESS photometry

TOI-1640 was observed by TESS during sectors 18, 19, 25, and 26 of its primary mission. The data was processed through the Science Processing Operations Center (SPOC; Jenkins et al. 2016), and transiting planet search algorithms (Jenkins 2002; Jenkins et al. 2010) detected a signal with a period of 1.9495 ± 0.000007 days and transit depth of 2185 ± 111 parts per million (ppm) in December 2019 based on the data from sector 18. After reviewing the results of the data validation reports (Twicken et al. 2018; Li et al. 2019), the TESS Science Office alerted TOI-1640 to the community on 14 January 2020¹.

We obtained the photometric light curve, corrected for systematics (PDC; Smith et al. 2012), from the Mikulski Archive for Space Telescopes² (MAST), using the `lightkurve`³ package (Lightkurve Collaboration et al. 2018). The data are shown in Fig. 1. We performed a period search using the Box-Fitting Least Squares (BLS; Kovács et al. 2002) and the Transit Least Squares (TLS; Hippke & Heller 2019) algorithms (Fig. A.1), and detected with both a signal with a period of 1.949 days and a signal detection efficiency (SDE) > 8 (empirical transit detection threshold from Aigrain et al. 2016). This period is the same as the one reported by the TESS SPOC.

Figure A.2 shows the TESS field of view and aperture size used for each of the four sectors for TOI-1640, generated using `tpfplotter`⁴ (Aller et al. 2020). No sources contaminating the TESS aperture are found in the *Gaia* DR2 catalog (Gaia Collaboration et al. 2018) down to a magnitude contrast limit of 6 mag compared to our target. Also, the *Gaia* EDR3 renormalized unit weight error (RUWE) value for this target is 1.26, below the critical value of 1.40 that is an indicator that a source is non-single or has a problematic astrometric solution (Lindgren et al. 2020).

2.2. High-spatial resolution imaging

In order to exclude the presence of close-by contaminants to our target, we observed LHS 1478 with the AstraLux high spatial resolution camera (Hormuth et al. 2008), located at the 2.2 m telescope of the Calar Alto Observatory (Almería, Spain). This instrument uses the lucky-imaging technique to obtain diffraction-limited images by obtaining thousands of short-exposure frames (below the atmospheric coherence time) to subsequently select the ones with the highest Strehl ratio (Strehl 1902) and combine them into a final high spatial resolution image. We observed this target on the night of 25 February 2020 under good weather conditions with a mean seeing of 1.0 arcsec. We obtained 41 710 frames with 20 ms exposure time for a total exposure of 83.4 s in the Sloan Digital Sky Survey z' filter (“SDSSz”), with a field-of-view windowed to 6×6 arcsec. The datacube was reduced by the instrument pipeline (Hormuth et al. 2008) and we selected the best-quality 10 % frames to produce the final high-resolution image. In order to obtain the sensitivity limits of the image, we used the `astrasens` package⁵ with the procedure described in Lillo-Box et al. (2012, 2014). Both the 5σ sensitivity curve and the image are shown in Fig. 2. We can exclude sources down to 0.2 arcsec with magnitude contrast of $\Delta z < 4$ mmag, corresponding to a maximum contamination level of 2.5 %.

We additionally estimate the probability of an undetected blended source in our high-spatial resolution image, called the blended source confidence (BSC), following the steps from in Lillo-Box et al. (2014). In short, we use a python implementation of this approach (`bsc`), which uses the TRILEGAL⁶ galactic model (v1.6, Girardi et al. 2012) to retrieve a simulated source population of the region around the corresponding target⁷. This simulated population is used to compute the density of stars around the target position (radius $r = 1$ deg) and derive the probability of chance-alignment at a given contrast magnitude and separation. We applied this to the position of LHS 1478, and use a maximum contrast magnitude of $\Delta m_{b,max} = 6.7$ mag in the z' passband, corresponding to the maximum contrast of a blended eclipsing binary that could mimic the observed transit depth. Thanks to our high-resolution image, we estimate the probability of an undetected blended source to be 0.2 %. The probability of such undetected source to be an appropriate eclipsing binary is even lower, and thus we conclude that the transit signal is not due to a blended eclipsing binary.

2.3. Ground-based photometry

Ground-based transit photometry was obtained to confirm the TESS transit event and to refine the ephemeris of the planet. We used the TESS Transit Finder, a customized version of the Tapir software package (Jensen 2013), to schedule our observations based on the preliminary ephemeris from the SPOC light curve. We obtained a total of three transit detections, which we include in our joint fit. The individual observations are described below.

2.3.1. MEarth-North

TOI-1640 was first observed by the MEarth-North telescope array on the 14 January 2020. MEarth-North is located at the Fred

¹ <https://tess.mit.edu/toi-releases/>

² <https://archive.stsci.edu>

³ <https://github.com/KeplerGO/Lightkurve>

⁴ <https://github.com/jlillo/tpfplotter>

⁵ <https://github.com/jlillo/astrasens>

⁶ <http://stev.oapd.inaf.it/cgi-bin/trilegal>

⁷ This is done in python by using the `astrobase` implementation by Bhatti et al. (2020).

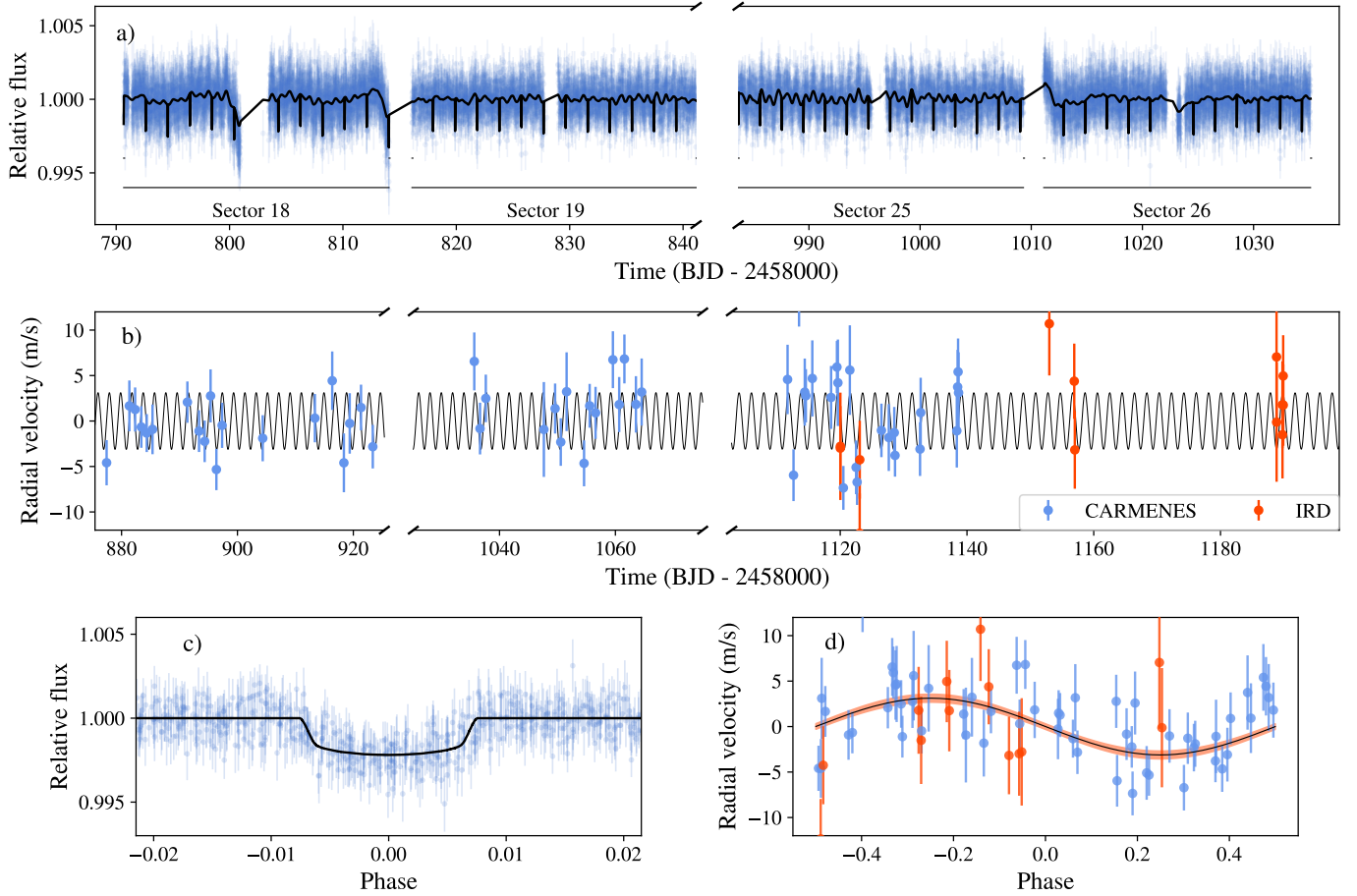


Fig. 1: Data and joint fit results with *juliet* (Sect. 3.2). a) TESS photometry for TOI-1640, with the black line representing the best transit + GP fit. b) Radial velocity data from CARMENES and IRD, with the jitter term added to the uncertainties. The black line is the best fit Keplerian model. c) Phased-folded TESS data, with the GP component removed. The black line is the best transit fit. d) Phased-folded RV data. The black line is the best fit Keplerian model, and the red-shaded area represents the 68% confidence interval.

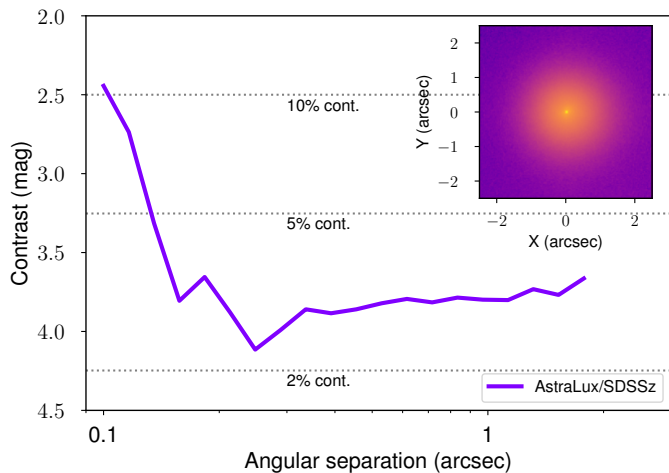


Fig. 2: AstraLux 5σ sensitivity curve (main panel) of the high-spatial resolution image obtained for LHS 1478 (inset) in the SDSS z' photometric band.

Lawrence Whipple Observatory on Mt. Hopkins, Arizona, and consists of eight 40 cm telescopes equipped with Apogee U42

cameras and custom RG715 passbands. We reduced the MEarth photometry following the standard procedures outlined in Irwin et al. (2007) and Berta et al. (2012), using a 6 arcsec aperture.

TOI-1640 was observed continuously with all eight telescopes from an airmass of 1.4 to 2.0 with 14-second exposures. The observations were taken through intermittent clouds and produced a tentative transit detection amid large residual systematics with a photometric dispersion of 4.2 parts-per-thousand (ppt). Although the combined light curve of the primary target TOI-1640 from all eight telescopes did not yield a reliable transit detection, these data were still used to rule out nearby eclipsing binaries in 101 of 103 sources within 2.5 arcmin and down to a differential magnitude of 8.6 mag. The two uncleared sources are faint ($\Delta = 3.8\text{--}4.0$ mag), and are blended with nearby sources. Their wide separations from TOI-1640 (1.8–2.2 arcmin) also make them improbable sources of the TESS transit events.

2.3.2. RCO

The first reliable ground-based detection of a transit of TOI-1640 was obtained on 31 January 2020 using the RCO 40 cm telescope located at the Grand-Pra Observatory near Valais Sion, Switzerland. We observed a full transit in the Sloan i' passband with an exposure time of 45 seconds. We used the *AstroImageJ* soft-

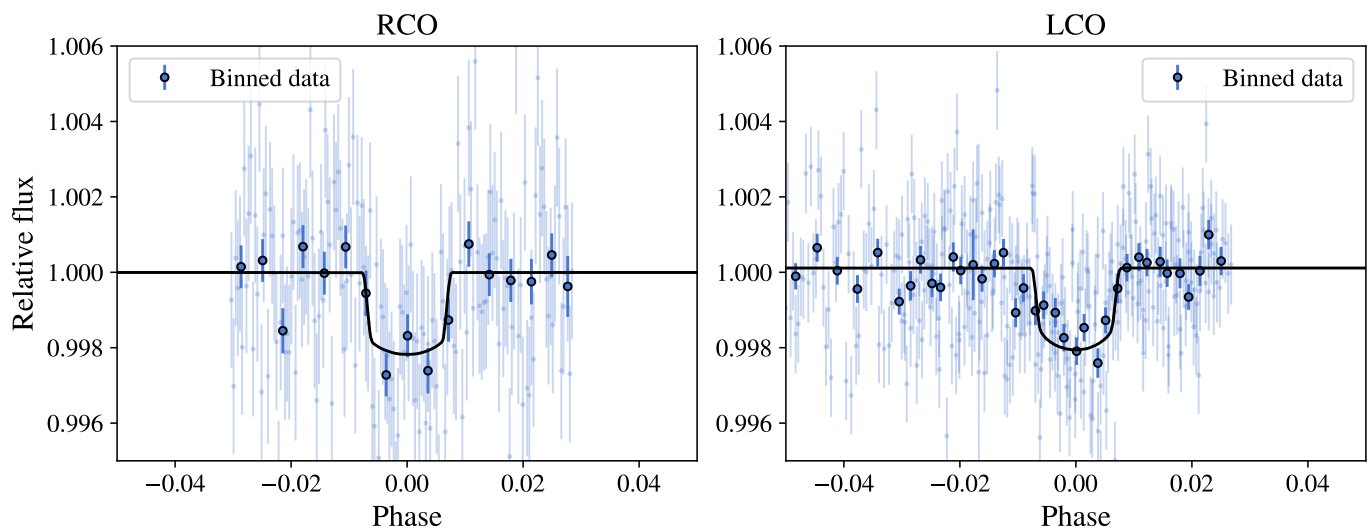


Fig. 3: Phased folded RCO (*left*) and LCOGT (*right*) data. The black line represents the best transit model from *juliet*. The small points show the raw data, while the large points show the data binned into 10 minute bins.

ware package (Collins et al. 2017) to perform differential photometry using 5.1 arcsec apertures, and to detrend against airmass to produce the light curve of TOI-1640 depicted in the left panel of Fig. 3. With our reduction, we achieved a photometric precision of 1.1 ppt in 3-minute bins. We detected the transit of TOI-1640 with a mid-transit time of ≈ 8 min late relative to the SPOC prediction (transit epoch was derived at the time using TESS data from sectors 18 and 19).

2.3.3. LCOGT

We observed two additional full transits of TOI-1640 on 27 August 2020 and 7 October 2020 from the Las Cumbres Observatory Global Telescope (LCOGT) (Brown et al. 2013) 1.0 m network node at McDonald Observatory. The images were calibrated by the standard LCOGT BANZAI pipeline (McCully et al. 2018).

Both light curves were obtained in the Pan-STARSS z -short passband with exposure times of 40 and 50 seconds in the August and October sequences, respectively. We used *AstroImageJ* to perform differential photometry using 5.8 arcsec apertures and to detrend against airmass. The resulting combined and phase folded light curves are included in the right panel of Fig. 3. With our reduction, we achieve photometric precisions of 0.7 ppt and 0.5 ppt in 3-minute bins, which resulted in a high S/N transit detection in each LCOGT light curve. Both LCOGT transit detections were at the time predicted by the refined ephemeris of TOI-1640 from the RCO detection.

2.4. Spectroscopy

2.4.1. CARMENES

We obtained a total of 57 spectra with CARMENES from 28 January 2020 to 16 October 2020, all taken with an exposure time of 1800 s. The visual channel (VIS) spectra were reduced with CARACAL (Zechmeister et al. 2014; Caballero et al. 2016b), and the radial velocities (RVs) were extracted using SERVAL (Zechmeister et al. 2018), along with selected activity indicators (Sect. 3.1). The RVs were corrected for barycentric motion,

instrumental drift, secular acceleration, and nightly zero-points (Tal-Or et al. 2019; Trifonov et al. 2020). The CARMENES RVs are shown in Fig. 1. A generalized Lomb-Scargle periodogram (GLS; Zechmeister & Kürster 2009) of the RV data shows a period at 1.949 days, consistent with the transit signal, with a theoretically computed False Alarm Probability (FAP) of less than 1% (Fig. 4). The CARMENES RVs are listed in Table A.1.

2.4.2. IRD spectroscopy

We observed LHS 1478 using the InfraRed Doppler (IRD) instrument at the Subaru 8.2 m telescope (Tamura et al. 2012; Kotani et al. 2018) between September and December 2020. A total of 13 spectra were obtained with an integration time of 900 s. IRD is a fiber-fed spectrograph and we injected light from the laser-frequency comb into the second fiber for the simultaneous wavelength calibration. The raw data were reduced into one-dimensional spectra using the IRAF software as well as a custom code (Kuzuhara et al. 2018; Hirano et al. 2020) to suppress the bias and correlated noise of the detectors. The typical signal-to-noise (S/N) ratio of the reduced spectra ranged from 60 to 95 per pixel at 1000 nm.

Following Hirano et al. (2020), we analyzed the observed spectra to extract precise RVs. In doing so, we combined multiple frames to obtain a high S/N template for the RV analysis, after removing the telluric lines as well as the instrumental profile of the spectrograph. The relative RV was then measured with respect to this template for each spectrum. The resulting relative RVs after the correction for the barycentric motion of Earth are listed in Table A.2 and shown in Fig. 1; the internal RV error was typically 3–6 m s^{-1} for each frame.

3. Analysis

3.1. Stellar parameters

The stellar parameters for this target were estimated using the CARMENES VIS stacked stellar template produced by SERVAL. T_{eff} , $\log g$, and iron abundance [Fe/H] were determined through spectral fitting with a grid of PHOENIX-SESAM models, fol-

Table 1: Stellar parameters of LHS 1478

Parameter	Value	Reference
Name	LHS 1478	Luy79
Karmn	J02573+765	
TOI	1640	ExoFOP-TESS
TIC	396562848	Sta18
α (J2000)	02 57 17.51	<i>Gaia</i> EDR3
δ (J2000)	+76 33 13.0	<i>Gaia</i> EDR3
SpT	M3.5 V	Cab16
J [mag]	9.615 ± 0.026	Skr06
G [mag]	12.2481 ± 0.0028	<i>Gaia</i> EDR3
T [mag]	11.0548 ± 0.0073	Sta19
ϖ [mas]	54.904 ± 0.018	<i>Gaia</i> EDR3
d [pc]	18.21 ± 0.01	<i>Gaia</i> EDR3
T_{eff} [K]	3381 ± 54	This work
$\log g$ [cgs]	4.87 ± 0.06	This work
[Fe/H] [dex]	-0.13 ± 0.19	This work
M_{\star} [M_{\odot}]	0.236 ± 0.012	This work
R_{\star} [R_{\odot}]	0.246 ± 0.008	This work
ρ_{\star} [g cm^{-3}] ^a	22.2 ± 2.5	This work
L_{\star} [$10^{-4} L_{\odot}$]	71.5 ± 1.2	Cif20
pEW _{Hα} [Å]	$+0.040 \pm 0.026$	This work
$v \sin i$ [km s^{-1}]	< 2	Mar21
P_{rot} [d]	[6.4] ^b	New16

References. Luy79: Luyten (1979); Sta18: Stassun et al. (2018); Cab16: Caballero et al. (2016a); Skr06: Skrutskie et al. (2006); *Gaia* EDR3: *Gaia* Collaboration et al. (2020); Sta19: Stassun et al. (2019); Cif20: Cifuentes et al. (2020); Mar21: Marfil et al., in prep; New16: Newton et al. (2016).

Notes. ^(a) Derived from M_{\star} and R_{\star} .

^(b) Flagged as a non-detection or undetermined detection by Newton et al. (2016).

lowing Passegger et al. (2019), using the upper limit $v \sin i = 2.0 \text{ km s}^{-1}$ of Reiners et al. (2018) and Marfil et al. (in prep.), who did not detect any rotational velocity. The luminosity L_{\star} was estimated by integrating the spectral energy distribution, with the photometric data used listed by Cifuentes et al. (2020). The stellar radius R_{\star} was determined through the Stefan–Boltzmann law, and the stellar mass M_{\star} through the mass-radius relation from Schweitzer et al. (2019). We estimated the overall activity level of the star from the pseudo-equivalent width of the H α line after subtraction of an inactive stellar template (pEW_{H α}) following Schöfer et al. (2019). We obtained a value of $+0.040 \pm 0.026 \text{ Å}$, which indicates that LHS 1478 is a fairly inactive star (Jeffers et al. 2018; Schöfer et al. 2019).

The star has a rotational period of 6.4 days, as listed by Newton et al. (2016), but the detection is deemed inconclusive. We looked at the SAP (Simple Aperture Photometry, Morris et al. 2020) and PDC data from TESS and, after masking the transits and performing a Lomb-Scargle periodogram, we could not detect any signal with a period of 6.4 days. We therefore agree with

Table 2: Posterior distributions from the joint fit. The uncertainties represent the 68% CI of the obtained distributions.

Parameter	Value
<i>Stellar density</i>	
ρ_{\star} [g cm^{-3}] ^a	$22.16^{+2.69}_{-2.27}$
<i>Orbital parameters</i>	
P [d]	$1.9495378^{+0.0000040}_{-0.0000041}$
T_0 [BJD]	$2458786.75425^{+0.00042}_{-0.00042}$
r_1 ^b	$0.811^{+0.008}_{-0.009}$
r_2 ^b	$0.046^{+0.001}_{-0.001}$
$p = R_p/R_{\star}$	$0.046^{+0.001}_{-0.001}$
$b = (a/R_{\star}) \cos i$	$0.717^{+0.012}_{-0.013}$
i [deg]	$87.45^{+0.05}_{-0.05}$
a/R_{\star}	$16.12^{+0.09}_{-0.09}$
K [m s^{-1}]	$3.13^{+0.23}_{-0.25}$
t_T [h]	$0.71^{+0.01}_{-0.01}$
<i>Derived planetary parameters</i>	
M_p [M_{\oplus}]	$2.33^{+0.20}_{-0.20}$
R_p [R_{\oplus}]	$1.24^{+0.05}_{-0.05}$
ρ_p [g cm^{-3}]	$6.66^{+1.08}_{-0.88}$
a [AU]	$0.01848^{+0.00061}_{-0.00063}$
T_{eq} [K] ^c	595^{+10}_{-9}

Notes. ^(a) Derived from lightcurve fitting, using the relations from Seager & Mallén-Ornelas (2003)

^(b) Parameterization from Espinoza (2018) for p and b .

^(c) Assuming zero Bond albedo.

Newton et al. (2016) in that the signal is a non-detection and may not correspond to the real rotational period for this star.

Time series of the activity indicators CRX, dLW, and H α (Zechmeister et al. 2018) were extracted from the spectra with SERVAL. We find no signs of periodic variations similar to the planet orbital period or the putative stellar rotational period of 6.4 days (Fig. 4). The only exception is for the H α data, where there is a signal at ≈ 6.8 days with at FAP = 5 %. This signal is not seen in any of the other indices or datasets and, therefore we cannot provide any insight to its origin or relevance. The activity data are not correlated with the RV data either, with correlation coefficient $|r| < 0.3$.

A summary of the stellar properties and relevant photometric and astrometric data from *Gaia* EDR3 is shown in Table 1.

3.2. Joint fit

We used juliet (Espinoza et al. 2019) to perform a joint fit of the TESS, RCO, LCOGT, CARMENES, and IRD data. We used the efficient, uninformative sampling scheme of Kipping (2013) to parameterize the limb-darkening in the TESS data, together with a quadratic law. For the RCO and LCOGT data we used a linear limb-darkening law. We also followed the parameterization presented in Espinoza (2018), with parameters r_1 and r_2 , to fit for p and b , the planet-to-star radius ratio and impact parameter, respectively. The TESS data were fitted separately

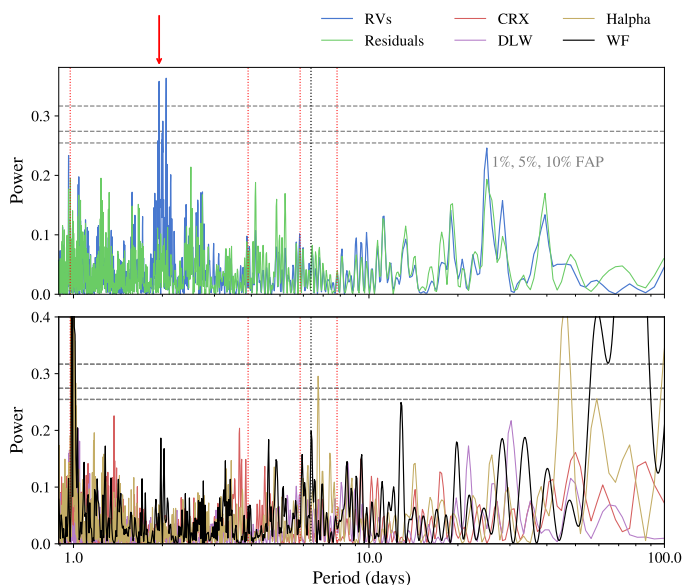


Fig. 4: GLS periodograms for the CARMENES RV and RV residuals from the fit (top panel), and activity indices plus window function (bottom panel). The window function was scaled down to have power comparable to the GLS periodograms. The dotted horizontal lines represent the 1%, 5%, and 10% FAP. The red arrow at the top is the position of the orbital period of the planet, and the red dotted vertical lines are aliases of that period. The black dotted vertical line represents the 6.4 days period from Newton et al. (2016).

by sector, each with its own relative flux offset and jitter, but we imposed identical limb-darkening coefficients for the transit curves from all sectors. We fitted the LCOGT data separately for each observing night, but as with the TESS data we imposed an identical limb-darkening coefficient for the two nights. The detrending of the TESS data was done by incorporating a Gaussian Process (GP) model; we used the `celerite` Matern kernel with hyperparameters (σ_{GP} , ρ_{GP}), the amplitude and time scale of the GP, respectively (Foreman-Mackey et al. 2017). The same GP model was used for each TESS sector. An initial search for the optimal parameters for this system was done with `exostriker` (Trifonov 2019), using all datasets, and the results were used to build the priors for `juliet`, which are shown in Table A.3. The obtained posterior probabilities are listed in Tables 2 and A.4.

We construct our full model, shown in Figs. 1 and 3, from the 68% confidence interval (CI) of the posterior distribution for each parameter. We find that the signal observed both in the photometric and RV data is consistent with a $2.33^{+0.20}_{-0.20} M_{\oplus}$ and $1.24^{+0.05}_{-0.05} R_{\oplus}$ planet, with a density of $6.66^{+1.08}_{-0.88} \text{ g cm}^{-3}$, orbiting the star with a period of $1.9495378^{+0.0000040}_{-0.0000041}$ days.

Since there is a brighter star ($G = 10.30$ mag) about 120 arcsec north of LHS 1478, we checked for possible contamination in the TESS light curve. We analyzed the transit data from TESS and LCOGT, using the GP-detrended data, leaving the dilution factor as a free parameter for the TESS data, and fixing the limb darkening coefficients to the values interpolated from limb darkening tables (Claret et al. 2013; Claret 2017). The parameters from Table 2 were very well recovered, and the best fit dilution factor is below 1%, and it is below 13% at 95% confidence. We conclude that the TESS light curve is therefore not contaminated.

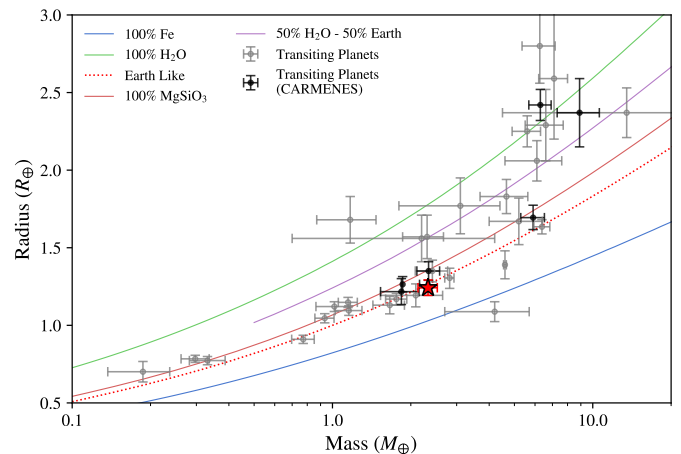


Fig. 5: Mass-radius diagram for LHS 1478 b (red star). The colored lines represent the composition models from Zeng et al. (2016, 2019). Transiting planets around M-dwarfs with mass and radius measurements are shown in black (detected with CARMENES) and gray circles.

A TLS search in the light curve residuals from the TESS data showed two significant periods at 13.9 and 27.8 days, but these are due to the sampling of the data (Fig. A.3). A GLS periodogram of the residuals of the RV data does not show any significant signals, either (Fig. 4).

4. Discussion and characterization prospects

Given the measured properties, we made a first exploratory guess of the planet composition. We compared its mass and radius with the models from Zeng et al. (2016, 2019), shown in Fig. 5, plus other transiting planets around M-dwarfs from the literature⁸. We find that LHS 1478 b is compatible with a bulk composition of $\sim 30\%$ Fe + 70% MgSiO₃, which makes it comparable to Earth's, thus strongly supporting the notion that it is a rocky world indeed.

Atmospheric characterization of rocky planets with (some) properties similar to Earth is one of the pivotal developments expected in the forthcoming years, thanks to the deployment of new ground and space-based facilities. The potential of a target for detailed characterization is a complicated function of the planet and host star properties, and the instrument to be used. In this sense, not all transiting planets that have interesting properties are equally suitable for actual characterization.

As a first approximation of the suitability of LHS 1478 b, we calculate the spectroscopic metrics from Kempton et al. (2018), which were developed to rank the best TESS targets for the instrumentation aboard the JWST. We estimate the emission spectroscopy metric (ESM) and transmission spectroscopy metric (TSM) to be 7.28 and 19.35, respectively. The upper panel of Figure 6 shows the ESMs of rocky exoplanets with measured masses, either through RVs or TTVs, and puts LHS 1478 b in that context. The ESM of 7.28 is slightly lower than the 7.5 threshold set by Kempton et al. (2018), but it is very close to that of Gl 1132 b, which is considered in that work as a benchmark rocky planet for emission spectroscopy. The lower panel illustrates TSM values. An acceptable TSM value for this class of planet is around 12 or higher (Table 1 in Kempton et al. 2018),

⁸ Data on transiting planets from <https://carmenes.caha.es/ext/tmp/>.

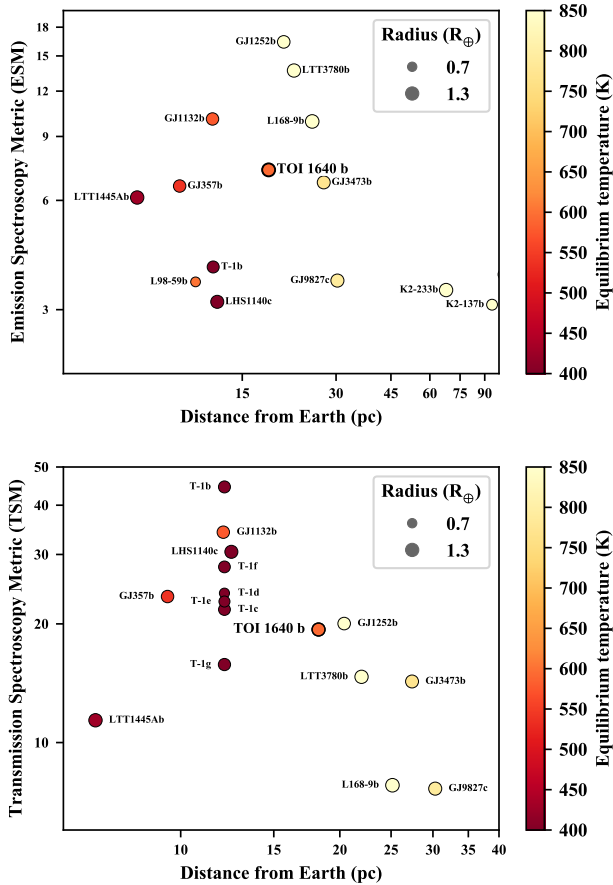


Fig. 6: Upper) The emission spectroscopy metric (ESM), and Lower) transmission spectroscopy metric (TSM) for exoplanets with a radius less than $1.5 R_{\oplus}$ and a mass determination by RVs or TTVs. LHS 1478 b (TOI-1640 b) is labeled and marked with thicker black borderline in both panels.

which implies that LHS 1478 b is likely an appropriate candidate for atmospheric characterization through transmission spectroscopy as well.

As a second refinement to its suitability for characterization, we assess the potential chemical species that could be detected in its atmosphere using near future instrumentation. Molecular features such as water, carbon dioxide, or methane should be typically observable on these kind of planets if they maintain a substantial atmosphere (Molaverdikhani et al. 2019a,b), but the detectability of such features can also be obscured by the presence of clouds (Molaverdikhani et al. 2020). In order to quantitatively assess the potential of atmospheric characterization observations of LHS 1478 b with the JWST, we calculate a few atmospheric models and their composition using the photo-chemical code ChemKM (Molaverdikhani et al. 2019a) and their corresponding spectra using petitRADTRANS (Mollière et al. 2019). We assumed a stellar radiation environment similar to that measured for the well-studied star GJ 667C ($T_{\text{eff}} \approx 3327$ K). For the model of the planetary atmospheric structure, we adapted a Venus-like temperature profile to make it consistent with the derived equilibrium temperature of the planet (see Table 2). Our photochemical models included 135 species and 788 reactions.

Figure 7 shows simulated realizations of the transmission spectrum of LHS 1478 b assuming solar (top panel) and 100 times enhanced metallicities (bottom panel). The dominant spec-

tral features come from water and methane, as expected, with a less extended CO_2 feature at around $4.5 \mu\text{m}$. The amplitudes of these features is between 50 to 100 ppm, which should be measurable given that the star is rather bright. This was verified using PANEXO (Batalha et al. 2017) simulations of the NIRISS-SOSS, NIRSpec-G395M, and MIRI-LRS instruments on board of JWST.

Hydrogen-dominated atmospheres with temperatures below 900 K are expected to have significant photochemically-produced hazes (e.g. He et al. 2018; Gao et al. 2020). If such a scenario applies to LHS 1478 b, it would result in the obscuration of spectral features, particularly in the case of an enhanced metallicity (see bottom panel in Figure 7). A relatively flat transmission spectrum might thus be indicative of a metallicity-enhanced atmosphere covered by haze, which might be indistinguishable from the planet having no atmosphere at all. If (a close to) flat spectrum was observed, ground-based high-resolution spectroscopy could then be used to detect unobscured molecular features and break the associated degeneracies.

In summary, the simulations in this section indicate that LHS 1478 b belongs to the small family of planets, along with GJ 357 b (Luque et al. 2019) and GJ 1132 b (Berta-Thompson et al. 2015), where we can realistically expect to obtain meaningful measurements and constraints with next-generation space telescopes such as JWST.

5. Conclusions

In this paper we have presented TESS and ground-based photometric observations, together with CARMENES and IRD Doppler spectroscopy, of the star LHS 1478. We determine LHS 1478 b to have a mass of $2.33^{+0.20}_{-0.19} M_{\oplus}$, a radius of $1.24^{+0.05}_{-0.05} R_{\oplus}$ and a bulk density of $6.69^{+1.02}_{-0.94} \text{g cm}^{-3}$, which is consistent with an Earth-like composition. The star is remarkably inactive, and we see no signs of additional planetary signals in the photometry or the radial velocities, thus greatly simplifying the analysis.

The equilibrium temperature of this planet places it in a recently found group of warm rocky planets, together with GJ 357 b and GJ 1132 b, which are ideal for atmospheric studies. The fact that the planetary signal is very isolated in both photometry and radial velocity, with no stellar activity or additional companions contaminating it, together with the proximity of the system to the Sun and the brightness of the star, make this an ideal target for near future transit observations with JWST and ground-based high-resolution spectrometers.

Acknowledgements. CARMENES is an instrument at the Centro Astronómico Hispano-Alemán (CAHA) at Calar Alto (Almería, Spain), operated jointly by the Junta de Andalucía and the Instituto de Astrofísica de Andalucía (CSIC). CARMENES was funded by the Max-Planck-Gesellschaft (MPG), the Consejo Superior de Investigaciones Científicas (CSIC), the Ministerio de Economía y Competitividad (MINECO) and the European Regional Development Fund (ERDF) through projects FICTS-2011-02, ICTS-2017-07-CAHA-4, and CAHA16-CE-3978, and the members of the CARMENES Consortium (Max-Planck-Institut für Astronomie, Instituto de Astrofísica de Andalucía, Landessternwarte Königstuhl, Institut de Ciències de l’Espai, Institut für Astrophysik Göttingen, Universidad Complutense de Madrid, Thüringer Landessternwarte Tautenburg, Instituto de Astrofísica de Canarias, Hamburger Sternwarte, Centro de Astrobiología and Centro Astronómico Hispano-Alemán), with additional contributions by the MINECO, the Deutsche Forschungsgemeinschaft through the Major Research Instrumentation Programme and Research Unit FOR2544 “Blue Planets around Red Stars”, the Klaus Tschira Stiftung, the states of Baden-Württemberg and Niedersachsen, and by the Junta de Andalucía. This work is partly financed by the Spanish Ministry of Economics and Competitiveness through project PGC2018-098153-B-C31. This paper includes data collected by the TESS mission. Funding for the TESS mission is provided by the NASA’s Science Mission Directorate. Resources supporting this work

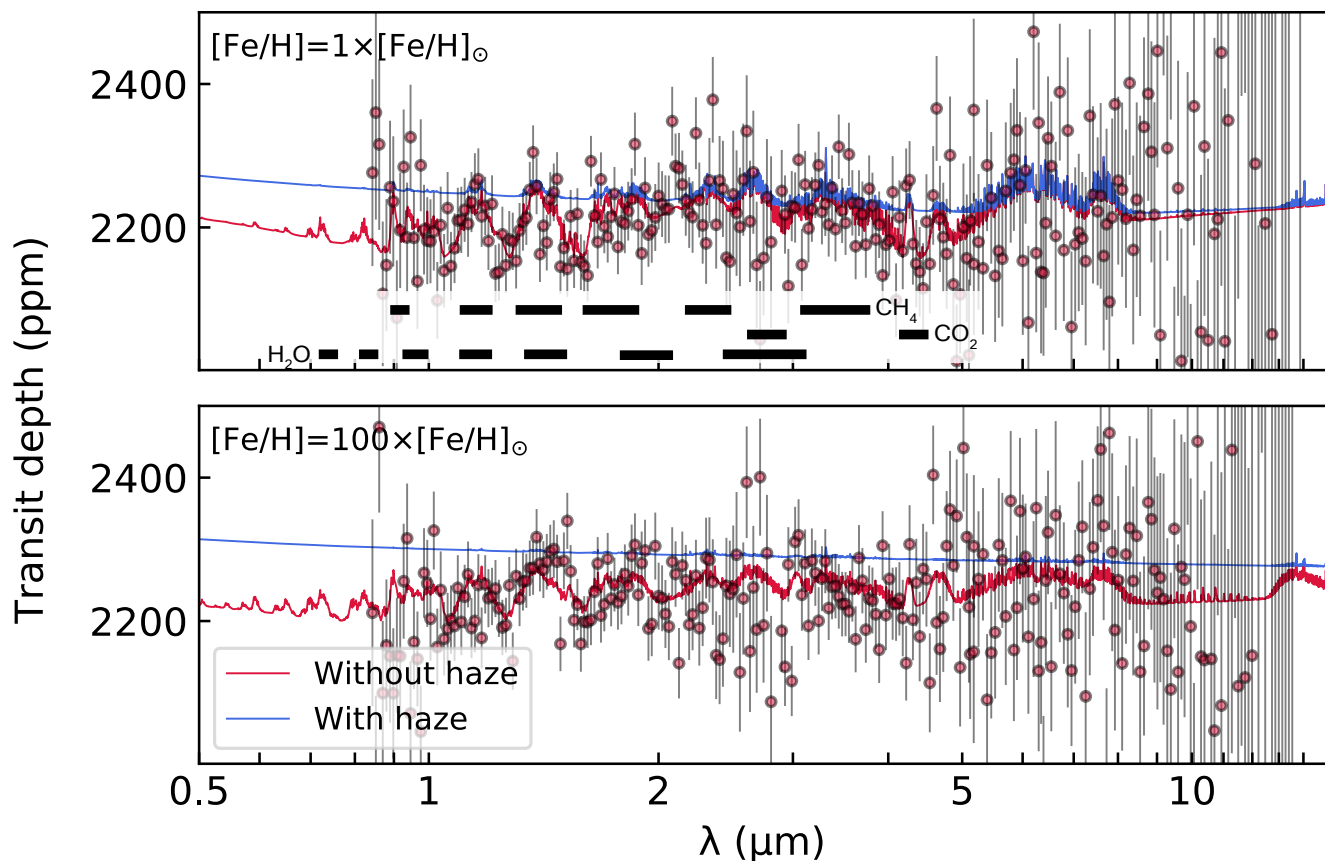


Fig. 7: Synthetic transmission atmospheric spectra of LHS 1478 b including haze opacity (solid blue lines) and without haze opacity (solid red lines). Simulated observations and estimated uncertainties are shown for the JWST NIRISS-SOSS, NIRSpec-G395M, and MIRI-LRS configurations, assuming two transits and binned for $R = 50$ (filled circles with error bars). Top : Fiducial models with solar abundance. Bottom : Metallicity enhanced by a factor of 100.

were provided by the NASA High-End Computing (HEC) Program through the NASA Advanced Supercomputing (NAS) Division at Ames Research Center for the production of the SPOC data products. This work makes use of observations from the LCOGT network. LCOGT telescope time was granted by NOIRLab through the Mid-Scale Innovations Program (MSIP). MSIP is funded by NSF. This work is partly supported by Grant-in-Aid for JSPS Fellows Grant Number JP20J21872, by JSPS KAKENHI Grant Numbers 22000005, JP15H02063, JP18H01265, JP18H05439, JP18H05442, JP19K14783, by JST PRESTO Grant Number JPMJPR1775, and by a University Research Support Grant from the National Astronomical Observatory of Japan (NAOJ).

References

- Aigrain, S., Parviainen, H., & Pope, B. J. S. 2016, *MNRAS*, 459, 2408
- Aller, A., Lillo-Box, J., Jones, D., Miranda, L. F., & Barceló Forteza, S. 2020, *A&A*, 635, A128
- Anglada-Escudé, G., Amado, P. J., Barnes, J., et al. 2016, *Nature*, 536, 437
- Astudillo-Defru, N., Cloutier, R., Wang, S. X., et al. 2020, *A&A*, 636, A58
- Batalha, N. E., Mandell, A., Pontoppidan, K., et al. 2017, *PASP*, 129, 064501
- Berta, Z. K., Irwin, J., Charbonneau, D., Burke, C. J., & Falco, E. E. 2012, *AJ*, 144, 145
- Berta-Thompson, Z. K., Irwin, J., Charbonneau, D., et al. 2015, *Nature*, 527, 204
- Bhatti, W., Bouma, L., Joshua, John, & Price-Whelan, A. 2020, *waqasbhatti/astrobase: astrobase v0.5.0*
- Bluhm, P., Luque, R., Espinoza, N., et al. 2020, *A&A*, 639, A132
- Brown, T. M., Baliber, N., Bianco, F. B., et al. 2013, *PASP*, 125, 1031
- Caballero, J. A., Cortés-Contreras, M., Alonso-Floriano, F. J., et al. 2016a, in 19th Cambridge Workshop on Cool Stars, Stellar Systems, and the Sun (CS19), 148
- Caballero, J. A., Guàrdia, J., López del Fresno, M., et al. 2016b, in Society of Photo-Optical Instrumentation Engineers (SPIE) Conference Series, Vol. 9910, *Observatory Operations: Strategies, Processes, and Systems VI*, ed. A. B. Peck, R. L. Seaman, & C. R. Benn, 99100E
- Cifuentes, C., Caballero, J. A., Cortés-Contreras, M., et al. 2020, *A&A*, 642, A115
- Claret, A. 2017, *A&A*, 600, A30
- Claret, A., Hauschildt, P. H., & Witte, S. 2013, *A&A*, 552, A16
- Collins, K. A., Kielkopf, J. F., Stassun, K. G., & Hessman, F. V. 2017, *AJ*, 153, 77
- Dreizler, S., Crossfield, I. J. M., Kossakowski, D., et al. 2020, *A&A*, 644, A127
- Espinoza, N. 2018, *RNAAS*, 2, 209
- Espinoza, N., Kossakowski, D., & Brahm, R. 2019, *MNRAS*, 490, 2262
- Foreman-Mackey, D., Agol, E., Ambikasaran, S., & Angus, R. 2017, *AJ*, 154, 220
- Gaia Collaboration, Brown, A. G. A., Vallenari, A., et al. 2018, *A&A*, 616, A1
- Gaia Collaboration, Brown, A. G. A., Vallenari, A., et al. 2020, *arXiv e-prints*, arXiv:2012.01533
- Gan, T., Shporer, A., Livingston, J. H., et al. 2020, *AJ*, 159, 160
- Gao, P., Thorngren, D. P., Lee, G. K., et al. 2020, *Nature Astronomy*, 1
- Gillon, M., Triaud, A. H. M. J., Demory, B.-O., et al. 2017, *Nature*, 542, 456
- Girardi, L., Barbieri, M., Groenewegen, M. A. T., et al. 2012, *Astrophysics and Space Science Proceedings*, 26, 165
- He, C., Hörst, S. M., Lewis, N. K., et al. 2018, *AJ*, 156, 38
- Hippke, M. & Heller, R. 2019, *A&A*, 623, A39
- Hirano, T., Kuzuhara, M., Kotani, T., et al. 2020, *PASJ*, 72, 93
- Horrmuth, F., Brandner, W., Hippler, S., & Henning, T. 2008, *Journal of Physics Conference Series*, 131, 012051
- Irwin, J., Irwin, M., Aigrain, S., et al. 2007, *MNRAS*, 375, 1449
- Jeffers, S. V., Schöfer, P., Lamert, A., et al. 2018, *A&A*, 614, A76
- Jenkins, J. M. 2002, *ApJ*, 575, 493

- Jenkins, J. M., Chandrasekaran, H., McCauliff, S. D., et al. 2010, in Society of Photo-Optical Instrumentation Engineers (SPIE) Conference Series, Vol. 7740, Software and Cyberinfrastructure for Astronomy, ed. N. M. Radziwill & A. Bridger, 77400D
- Jenkins, J. M., Twicken, J. D., McCauliff, S., et al. 2016, in Society of Photo-Optical Instrumentation Engineers (SPIE) Conference Series, Vol. 9913, Software and Cyberinfrastructure for Astronomy IV, ed. G. Chiozzi & J. C. Guzman, 99133E
- Jensen, E. 2013, Tapir: A web interface for transit/eclipse observability
- Kanodia, S., Cañas, C. I., Stefansson, G., et al. 2020, *ApJ*, 899, 29
- Kemmer, J., Stock, S., Kossakowski, D., et al. 2020, *A&A*, 642, A236
- Kempton, E. M. R., Bean, J. L., Louie, D. R., et al. 2018, *PASP*, 130, 114401
- Kipping, D. M. 2013, *MNRAS*, 435, 2152
- Kotani, T., Tamura, M., Nishikawa, J., et al. 2018, in Proc. SPIE, Vol. 10702, Ground-based and Airborne Instrumentation for Astronomy VII, 1070211
- Kovács, G., Zucker, S., & Mazeh, T. 2002, *A&A*, 391, 369
- Kuzuhara, M., Hirano, T., Kotani, T., et al. 2018, in Proc. SPIE, Vol. 10702, Ground-based and Airborne Instrumentation for Astronomy VII, 1070260
- Li, J., Tenenbaum, P., Twicken, J. D., et al. 2019, *PASP*, 131, 024506
- Lightkurve Collaboration, Cardoso, J. V. d. M., Hedges, C., et al. 2018, Lightkurve: Kepler and TESS time series analysis in Python, Astrophysics Source Code Library
- Lillo-Box, J., Barrado, D., & Bouy, H. 2012, *A&A*, 546, A10
- Lillo-Box, J., Barrado, D., & Bouy, H. 2014, *A&A*, 566, A103
- Lindgren, L., Klioner, S. A., Hernández, J., et al. 2020, arXiv e-prints, arXiv:2012.03380
- Luque, R., Nowak, G., Pallé, E., et al. 2018, *A&A*, 620, A171
- Luque, R., Pallé, E., Kossakowski, D., et al. 2019, *A&A*, 628, A39
- Luyten, W. J. 1979, LHS catalogue. A catalogue of stars with proper motions exceeding 0.5'' annually
- McCully, C., Volgenau, N. H., Harbeck, D.-R., et al. 2018, in Society of Photo-Optical Instrumentation Engineers (SPIE) Conference Series, Vol. 10707, Software and Cyberinfrastructure for Astronomy V, ed. J. C. Guzman & J. Ibsen, 107070K
- Molaverdikhani, K., Henning, T., & Mollière, P. 2019a, *ApJ*, 883, 194
- Molaverdikhani, K., Henning, T., & Mollière, P. 2019b, *ApJ*, 873, 32
- Molaverdikhani, K., Henning, T., & Mollière, P. 2020, *ApJ*, 899, 53
- Mollière, P., Wardenier, J., van Boekel, R., et al. 2019, *A&A*, 627, A67
- Morris, R. L., Twicken, J. D., Smith, J. C., et al. 2020, Kepler Data Processing Handbook: Photometric Analysis, Kepler Science Document KSCI-19081-003
- Newton, E. R., Irwin, J., Charbonneau, D., et al. 2016, *ApJ*, 821, 93
- Nowak, G., Luque, R., Parviainen, H., et al. 2020, *A&A*, 642, A173
- Passegger, V. M., Schweitzer, A., Shulyak, D., et al. 2019, *A&A*, 627, A161
- Quirrenbach, A., Amado, P. J., Caballero, J. A., et al. 2016, in Society of Photo-Optical Instrumentation Engineers (SPIE) Conference Series, Vol. 9908, Ground-based and Airborne Instrumentation for Astronomy VI, ed. C. J. Evans, L. Simard, & H. Takami, 990812
- Rackham, B. V., Apai, D., & Giampapa, M. S. 2018, *ApJ*, 853, 122
- Reiners, A., Zechmeister, M., Caballero, J. A., et al. 2018, *A&A*, 612, A49
- Ricker, G. R., Winn, J. N., Vanderspek, R., et al. 2015, *JATIS*, 1, 014003
- Schöfer, P., Jeffers, S. V., Reiners, A., et al. 2019, *A&A*, 623, A44
- Schweitzer, A., Passegger, V. M., Cifuentes, C., et al. 2019, *A&A*, 625, A68
- Seager, S., & Mallén-Ornelas, G. 2003, *ApJ*, 585, 1038
- Skrutskie, M. F., Cutri, R. M., Stiening, R., et al. 2006, *AJ*, 131, 1163
- Smith, J. C., Stumpe, M. C., Van Cleve, J. E., et al. 2012, *PASP*, 124, 1000
- Stassun, K. G., Oelkers, R. J., Paegert, M., et al. 2019, *AJ*, 158, 138
- Stassun, K. G., Oelkers, R. J., Pepper, J., et al. 2018, *AJ*, 156, 102
- Stock, S., Nagel, E., Kemmer, J., et al. 2020, *A&A*, 643, A112
- Strehl, K. 1902, *Astronomische Nachrichten*, 158, 89
- Tal-Or, L., Trifonov, T., Zucker, S., Mazeh, T., & Zechmeister, M. 2019, *MNRAS*, 484, L8
- Tamura, M., Suto, H., Nishikawa, J., et al. 2012, in Proc. SPIE, Vol. 8446, Ground-based and Airborne Instrumentation for Astronomy IV, 84461T
- Trifonov, T. 2019, The Exo-Striker: Transit and radial velocity interactive fitting tool for orbital analysis and N-body simulations
- Trifonov, T., Tal-Or, L., Zechmeister, M., et al. 2020, *A&A*, 636, A74
- Twicken, J. D., Catanzarite, J. H., Clarke, B. D., et al. 2018, *PASP*, 130, 064502
- Zechmeister, M., Anglada-Escudé, G., & Reiners, A. 2014, *A&A*, 561, A59
- Zechmeister, M., Dreizler, S., Ribas, I., et al. 2019, *A&A*, 627, A49
- Zechmeister, M. & Kürster, M. 2009, *A&A*, 496, 577
- Zechmeister, M., Reiners, A., Amado, P. J., et al. 2018, *A&A*, 609, A12
- Zeng, L., Jacobsen, S. B., Sasselov, D. D., et al. 2019, *PNAS*, 116, 9723
- Zeng, L., Sasselov, D. D., & Jacobsen, S. B. 2016, *ApJ*, 819, 127
- 1 School of Physics and Astronomy, Queen Mary University London, 327 Mile End Road, London E1 4NS, UK
- 2 Institut de Ciències de l'Espai (ICE, CSIC), Campus UAB, Can Magrans s/n, 08193 Bellaterra, Spain
- 3 Institut d'Estudis Espacials de Catalunya (IEEC), 08034 Barcelona, Spain
- 4 Institut für Astrophysik, Georg-August-Universität, Friedrich-Hund-Platz 1, 37077 Göttingen, Germany
- 5 Landessternwarte, Zentrum für Astronomie der Universität Heidelberg, Königstuhl 12, 69117 Heidelberg, Germany
- 6 Max-Planck-Institut für Astronomie, Königstuhl 17, 69117 Heidelberg, Germany
- 7 Instituto de Astrofísica de Andalucía (IAA-CSIC), Glorieta de la Astronomía s/n, 18008 Granada, Spain
- 8 Centro de Astrobiología (CSIC-INTA), ESAC, Camino bajo del castillo s/n, 28692 Villanueva de la Cañada, Madrid, Spain
- 9 Instituto de Astrofísica de Canarias, 38205 La Laguna, Tenerife, Spain
- 10 Departamento de Astrofísica, Universidad de La Laguna, 38206 La Laguna, Tenerife, Spain
- 11 Space Telescope Science Institute, 3700 San Martin Drive, Baltimore, MD 21218, USA
- 12 Komaba Institute for Science, The University of Tokyo, 3-8-1 Komaba, Meguro, Tokyo 153-8902, Japan
- 13 Japan Science and Technology Agency, PRESTO, 3-8-1 Komaba, Meguro, Tokyo 153-8902, Japan
- 14 Astrobiology Center, 2-21-1 Osawa, Mitaka, Tokyo 181-8588, Japan
- 15 Department of Earth and Planetary Science, The University of Tokyo, Tokyo, Japan
- 16 National Astronomical Observatory of Japan, 2-21-1 Osawa, Mitaka, Tokyo 181-8588, Japan
- 17 SETI Institute, Mountain View, CA 94043, USA
- 18 NASA Ames Research Center, Moffett Field, CA 94035, USA
- 19 Center for Astrophysics | Harvard & Smithsonian, 60 Garden St, Cambridge, MA, 02138, USA
- 20 Grand Pra Observatory, Switzerland
- 21 Observatori Astronòmic Albanyà, Camí de Bassegoda S/N, Albanyà 17733, Girona, Spain
- 22 Subaru Telescope, 650 N. Aohoku Place, Hilo, HI 96720, USA
- 23 Thüringer Landessternwarte Tautenburg, Sternwarte 5, 07778 Tautenburg, Germany
- 24 Department of Physics & Astronomy, Swarthmore College, Swarthmore PA 19081, USA
- 25 Department of Astronomy, School of Science, The Graduate University for Advanced Studies (SOKENDAI), 2-21-1 Osawa, Mitaka, Tokyo, Japan
- 26 MIT Kavli Institute for Astrophysics and Space Research, Massachusetts Institute of Technology, Cambridge, MA 02139, USA
- 27 Departamento de Física de la Tierra y Astrofísica and IPARCOS-UCM (Instituto de Física de Partículas y del Cosmos de la UCM), Facultad de Ciencias Físicas, Universidad Complutense de Madrid, 28040, Madrid, Spain
- 28 Department of Astronomy, The University of Tokyo, 7-3-1 Hongo, Bunkyo-ku, Tokyo 113-0033, Japan
- 29 Centro Astronómico Hispano-Alemán, Observatorio de Calar Alto, 04550 Gérgal, Almería, Spain
- 30 Hamburger Sternwarte, Universität Hamburg, Gojenbergsweg 112, 21029 Hamburg, Germany
- 31 Homer L. Dodge Department of Physics and Astronomy, University of Oklahoma, 440 West Brooks Street, Norman, OK 73019, USA
- 32 Department of Earth, Atmospheric and Planetary Sciences, Massachusetts Institute of Technology, Cambridge, MA 02139, USA
- 33 NASA Goddard Space Flight Center, 8800 Greenbelt Rd, Greenbelt, MD 20771, USA
- 34 Hazelwood Observatory, Australia
- 35 Planetary Discoveries, Fredericksburg, VA 22405, USA

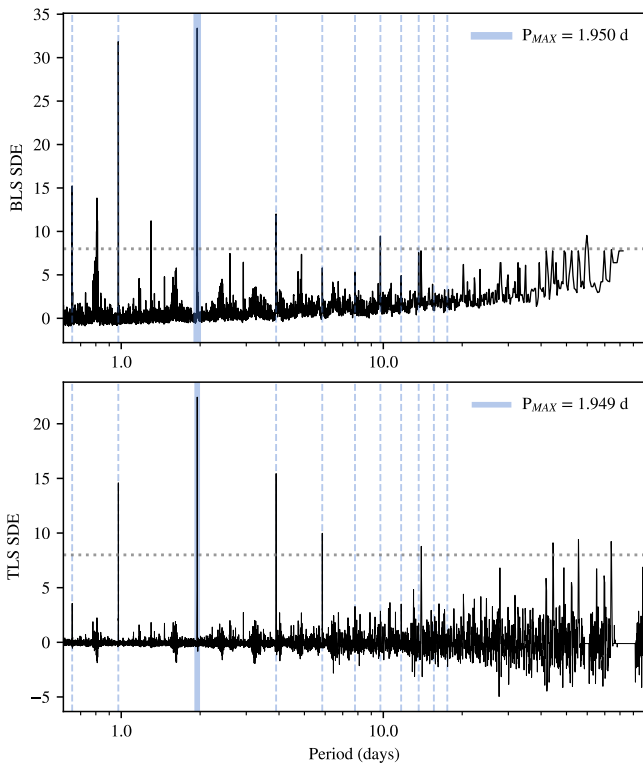


Fig. A.1: BLS (top panel) and TLS (bottom panel) signal detection efficiency (SDE) for the TESS light curve. The vertical blue lines correspond to aliases of the maximum period, highlighted by the blue-shaded region. The dashed horizontal line in both panels corresponds to the threshold for transit detection ($SDE > 8$) from [Aigrain et al. \(2016\)](#).

Appendix A: Additional figures and tables

Table A.1: Radial velocity data and activity indicators from CARMENES VIS.

BJD -2450000	RV m s^{-1}	RV error m s^{-1}	CRX $\text{m s}^{-1} \text{Np}^{-1}$	dLW $\text{m}^2 \text{s}^{-2}$	H α
8877.420	-4.54	2.03	11.0 ± 17.8	3.3 ± 2.4	0.934 ± 0.003
8881.348	1.71	2.40	2.0 ± 25.8	-20.4 ± 4.2	0.943 ± 0.004
8882.344	1.31	1.96	-8.3 ± 20.0	3.4 ± 1.8	0.930 ± 0.003
8883.412	-0.62	1.78	-8.0 ± 17.4	4.0 ± 1.9	0.925 ± 0.003
8884.348	-1.28	1.52	4.9 ± 14.8	8.2 ± 1.9	0.943 ± 0.003
8885.346	-0.87	2.33	-3.2 ± 23.4	9.3 ± 2.2	0.968 ± 0.004
8891.361	2.12	1.77	-1.9 ± 17.9	4.6 ± 1.6	0.949 ± 0.003
8893.372	-1.07	1.80	-22.7 ± 16.9	3.8 ± 1.9	0.923 ± 0.003
8894.345	-2.19	1.78	-15.2 ± 14.8	6.0 ± 1.8	0.930 ± 0.003
8895.364	2.81	2.54	-50.7 ± 25.3	-8.6 ± 2.1	0.925 ± 0.004
8896.368	-5.29	1.77	15.4 ± 18.2	-4.6 ± 2.1	0.933 ± 0.003
8897.353	-0.43	2.03	2.0 ± 21.8	-1.4 ± 1.9	0.928 ± 0.004
8904.361	-1.85	2.09	12.2 ± 18.9	-0.7 ± 2.0	0.937 ± 0.004
8913.365	0.36	2.24	-26.4 ± 22.9	0.9 ± 3.0	0.919 ± 0.004
8916.359	4.48	2.88	-58.1 ± 29.3	4.8 ± 4.0	0.920 ± 0.005
8918.371	-4.55	2.90	39.2 ± 30.7	43.1 ± 5.2	0.929 ± 0.005
8919.376	-0.22	3.00	13.4 ± 31.9	-9.4 ± 3.0	0.920 ± 0.005
8921.328	1.53	2.07	-0.6 ± 19.3	-4.8 ± 2.5	0.916 ± 0.003
8923.357	-2.78	1.92	8.2 ± 18.2	-2.6 ± 2.1	0.916 ± 0.003
9035.645	6.60	2.85	-43.2 ± 29.6	22.8 ± 4.5	0.917 ± 0.005
9036.639	-0.79	2.46	-32.8 ± 25.1	8.7 ± 2.4	0.907 ± 0.003
9037.633	2.53	2.19	12.1 ± 22.8	0.9 ± 1.8	0.920 ± 0.003
9047.655	-0.89	5.02	-28.1 ± 27.8	3.5 ± 2.2	0.908 ± 0.003
9049.595	1.42	2.35	17.0 ± 24.5	-7.1 ± 2.3	0.909 ± 0.004
9050.571	-2.27	2.19	-10.2 ± 19.9	-11.9 ± 2.7	0.901 ± 0.003
9051.580	3.27	4.09	-38.8 ± 41.5	-31.8 ± 5.5	0.922 ± 0.007
9054.590	-4.61	2.08	-50.6 ± 18.2	-0.5 ± 1.7	0.915 ± 0.003
9055.559	1.72	1.94	14.1 ± 18.3	-3.1 ± 2.3	0.912 ± 0.003
9056.575	0.94	2.48	5.6 ± 23.8	-7.8 ± 2.3	0.917 ± 0.004
9059.567	6.79	2.78	27.8 ± 28.9	-4.5 ± 2.4	0.932 ± 0.004
9060.656	1.85	2.67	18.2 ± 26.4	1.1 ± 2.9	0.924 ± 0.004
9061.554	6.87	2.28	-18.4 ± 22.1	4.3 ± 2.6	0.931 ± 0.004
9063.543	1.87	2.75	32.5 ± 29.1	10.0 ± 3.1	0.915 ± 0.005
9064.535	3.23	3.40	-18.5 ± 36.9	13.3 ± 3.6	0.920 ± 0.005
9111.691	4.61	3.54	47.2 ± 35.5	-4.9 ± 4.7	0.957 ± 0.007
9112.631	-5.92	2.46	25.0 ± 21.9	-1.8 ± 1.8	0.946 ± 0.004
9113.501	14.85	4.18	112.7 ± 42.5	-37.7 ± 6.8	0.947 ± 0.007
9114.403	3.22	3.41	67.2 ± 35.4	-22.7 ± 5.1	0.946 ± 0.005
9114.577	2.82	2.55	46.3 ± 24.7	-2.9 ± 2.3	0.939 ± 0.004
9115.595	4.73	3.93	94.9 ± 38.6	-1.9 ± 4.4	0.950 ± 0.006
9118.556	2.63	3.15	95.2 ± 27.2	-26.8 ± 5.0	0.947 ± 0.005
9119.480	5.98	2.49	10.0 ± 23.1	-4.0 ± 3.0	0.934 ± 0.004
9119.630	4.25	4.54	16.5 ± 49.0	-5.5 ± 4.7	0.947 ± 0.007
9120.495	-7.31	1.94	-2.1 ± 18.8	-0.6 ± 2.0	0.943 ± 0.003
9121.516	5.64	4.71	84.5 ± 49.1	48.3 ± 6.1	0.937 ± 0.008
9122.504	-5.05	2.59	42.6 ± 26.9	36.5 ± 4.1	0.935 ± 0.005
9122.662	-6.68	2.06	15.7 ± 21.2	-3.7 ± 2.8	0.920 ± 0.004
9126.500	-0.99	2.57	31.7 ± 24.1	1.2 ± 3.2	0.948 ± 0.005
9127.662	-1.77	3.39	64.7 ± 32.3	5.6 ± 3.2	0.943 ± 0.005
9128.527	-1.24	2.44	-32.1 ± 23.6	1.9 ± 1.7	0.941 ± 0.003
9128.644	-3.74	1.85	-5.5 ± 16.6	3.7 ± 1.7	0.931 ± 0.003
9132.594	-3.04	2.59	41.0 ± 24.1	-1.5 ± 2.4	0.918 ± 0.003
9132.694	0.97	3.56	64.1 ± 35.5	10.3 ± 3.5	0.905 ± 0.006
9138.394	-1.04	3.77	-69.0 ± 37.3	-0.1 ± 3.6	0.943 ± 0.006
9138.528	3.79	3.83	63.5 ± 38.4	-1.3 ± 4.2	0.930 ± 0.006
9138.595	5.45	3.38	-105.6 ± 30.0	-7.7 ± 4.0	0.915 ± 0.006
9138.672	3.15	4.22	-20.2 ± 44.0	-3.6 ± 3.5	0.913 ± 0.007

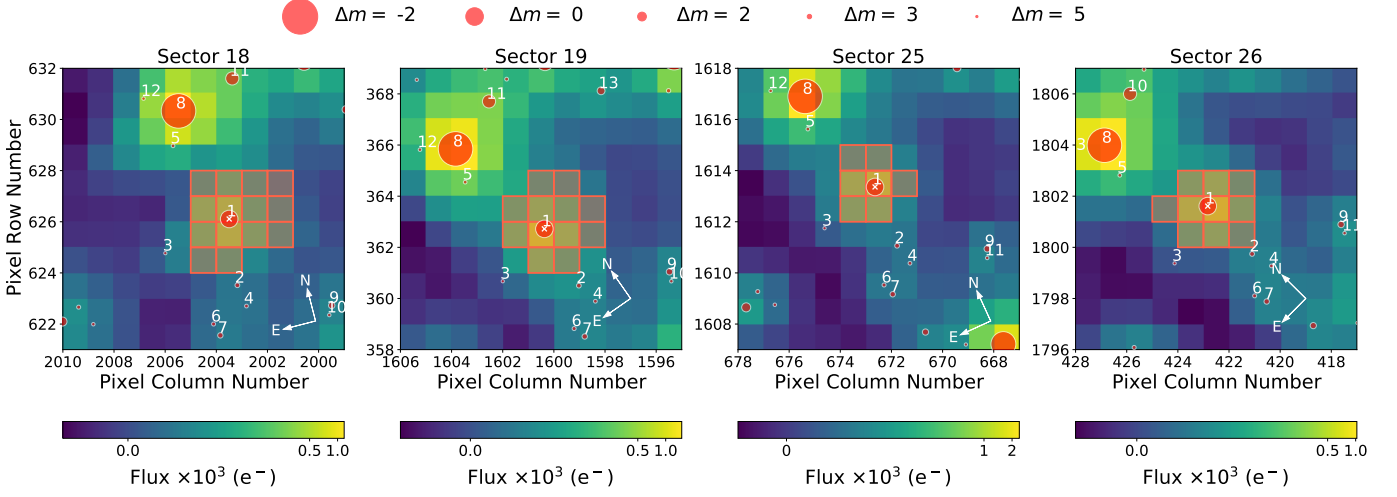


Fig. A.2: TESS target pixel files for all four sectors that observed the target TOI-1640. The red-shaded area corresponds to the apertures used to extract the photometry. The nearest sources to the target with up to 6 magnitude difference from Gaia are marked with red circles. TESS pixel scale is ~ 21 arcsec.

Table A.2: Radial velocity data from IRD.

BJD	RV	RV error
-2450000	m s^{-1}	m s^{-1}
9120.014	-3.25	3.78
9120.024	-3.05	5.27
9123.071	-12.62	3.49
9123.082	-4.52	3.36
9152.992	10.43	5.03
9156.926	4.11	3.16
9157.012	-3.44	3.34
9188.842	6.78	6.78
9188.853	-0.39	5.99
9189.771	1.52	3.97
9189.781	-1.77	4.00
9189.890	4.69	3.60
9189.901	1.49	3.60

Table A.3: Priors used for the juliet run.

Parameter	Prior ^a
M_{lc}^b [ppm]	$\mathcal{N}(0, 0.1)$
σ_{lc}^b [ppm]	$\mathcal{LU}(0.1, 1000)$
$q_{1,\text{TESS}}$	$\mathcal{U}(0, 1)$
$q_{2,\text{TESS}}$	$\mathcal{U}(0, 1)$
$q_{1,\text{LCO,RCO}}$	$\mathcal{U}(0, 1)$
μ_{RV} [m s^{-1}] ^c	$\mathcal{N}(0, 0.2)$
σ_{RV} [m s^{-1}] ^c	$\mathcal{LU}(10^{-4}, 15)$
P [d]	$\mathcal{N}(1.949, 0.01)$
T_0 [BJD-2458000]	$\mathcal{N}(786, 0.01)$
r_1	$\mathcal{U}(0, 1)$
r_2	$\mathcal{U}(0, 1)$
a/R_\star	$\mathcal{N}(16.1, 0.2)$
K [m s^{-1}]	$\mathcal{U}(0.2, 10)$
e	Fixed(0)
$\sigma_{\text{GP, TESS}}$ [ppm]	$\mathcal{LU}(10^{-6}, 10^6)$
$\rho_{\text{GP, TESS}}$ [d]	$\mathcal{LU}(10^{-3}, 10^3)$

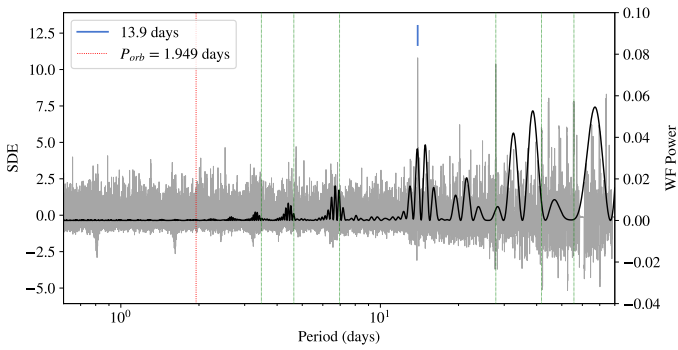


Fig. A.3: TLS of the TESS light curve residuals, after subtracting the GP+transit model. The dashed green lines are the aliases of the 13.9 days signal. The black line represents the window function of the data.

Notes. ^(a) \mathcal{N} : Normal distribution, \mathcal{LU} : Log-Uniform distribution, \mathcal{U} : Uniform distribution.

^(b) The same prior distributions were assumed for the photometric data, where lc stands for TESS sectors 18, 19, 25, 26, the two nights of photometry from LCOGT, and RCO.

^(c) The same prior distributions were assumed for the radial velocity data, where RV stands for CARMENES and IRD.

Table A.4: Posterior distributions for the instrumental parameters. The uncertainties represent the 68 % CI of the obtained distributions.

Parameter	Value
<i>Photometric parameters</i>	
M_{S18} [10^{-6} ppm]	$3.97^{+57.05}_{-56.47}$
σ_{S18} [ppm]	$1.78^{+11.24}_{-1.51}$
M_{S19} [10^{-6} ppm]	$-16.15^{+52.67}_{-50.37}$
σ_{S19} [ppm]	$1.99^{+12.69}_{-1.68}$
M_{S25} [10^{-6} ppm]	$-75.50^{+51.51}_{-50.25}$
σ_{S25} [ppm]	$2.04^{+13.31}_{-1.75}$
M_{S26} [10^{-6} ppm]	$-12.42^{+53.02}_{-56.05}$
σ_{S26} [ppm]	$1.91^{+11.40}_{-1.63}$
M_{LCO1} [10^{-6} ppm]	$-115.66^{+104.37}_{-103.52}$
σ_{LCO1} [ppm]	$977.77^{+16.31}_{-30.72}$
M_{LCO2} [10^{-6} ppm]	$-69.46^{+125.09}_{-123.14}$
σ_{LCO2} [ppm]	$856.87^{+90.00}_{-107.94}$
M_{RCO} [10^{-6} ppm]	$10.19^{+144.64}_{-143.99}$
σ_{RCO} [ppm]	$651.31^{+250.94}_{-641.52}$
$q_{1,TESS}^a$	$0.29^{+0.21}_{-0.16}$
$q_{2,TESS}^a$	$0.43^{+0.34}_{-0.29}$
$q_{1,LCO}$	$0.51^{+0.26}_{-0.28}$
$q_{1,RCO}$	$0.34^{+0.31}_{-0.23}$
<i>RV parameters</i>	
$\mu_{CARMENES}$ [$m s^{-1}$]	$0.04^{+0.17}_{-0.16}$
$\sigma_{CARMENES}$ [$m s^{-1}$]	$1.43^{+0.56}_{-0.70}$
μ_{IRD} [$m s^{-1}$]	$-0.26^{+0.43}_{-0.44}$
σ_{IRD} [$m s^{-1}$]	$2.66^{+1.46}_{-1.91}$
<i>GP parameters</i>	
$GP_{\sigma,TESS}$ [10^{-6} ppm]	$339.76^{+20.12}_{-19.07}$
$GP_{\rho,TESS}$ [d]	$0.25^{+0.02}_{-0.02}$

Notes. ^(a) Parameterization from [Kipping \(2013\)](#).